

# Physics-informed DeepCT: Sinogram Wavelet Decomposition Meets Masked Diffusion

Zekun Zhou, Tan Liu, Bing Yu, Yanru Gong, Liu Shi, Qiegen Liu, *Senior Member, IEEE*

**Abstract**—Diffusion model shows remarkable potential on sparse-view computed tomography (SVCT) reconstruction. However, when a network is trained on a limited sample space, its generalization capability may be constrained, which degrades performance on unfamiliar data. For image generation tasks, this can lead to issues such as blurry details and inconsistencies between regions. To alleviate this problem, we propose a Sinogram-based Wavelet random decomposition And Random mask diffusion Model (SWARM) for SVCT reconstruction. Specifically, introducing a random mask strategy in the sinogram effectively expands the limited training sample space. This enables the model to learn a broader range of data distributions, enhancing its understanding and generalization of data uncertainty. In addition, applying a random training strategy to the high-frequency components of the sinogram wavelet enhances feature representation and improves the ability to capture details in different frequency bands, thereby improving performance and robustness. Two-stage iterative reconstruction method is adopted to ensure the global consistency of the reconstructed image while refining its details. Experimental results demonstrate that SWARM outperforms competing approaches in both quantitative and qualitative performance across various datasets.

**Index Terms**—Sparse-view CT, random mask, sinogram wavelet decomposition, diffusion model.

## I. INTRODUCTION

**S**PARSE-VIEW X-ray computed tomography (SVCT) is extensively studied for its low-dose and rapid imaging benefits in medical diagnosis and industrial non-destructive testing [1], [2]. However, due to the incomplete of data acquisition of SVCT, serious artifacts are introduced into the reconstructed images, obscuring important internal structures and features [3]. SVCT reconstruction is a challenging inverse problem and improving the reconstruction quality has been a frontier in recent years [4].

Classical iterative reconstruction methods [5] were proposed to improve the image quality though the performance was still poor on highly sparse views. Compressed sensing [6] utilized priors applicable to sparse data such as total variation (TV) [7], [8] and wavelet frame [9], demonstrating a powerful ability to data with sparsity. However, these methods are computationally expensive due to the iterative update steps required and the effect is limited by the parameter sensitivity [10], [11].

This work was supported by National Natural Science Foundation of China (621220033, 62201193). (Z. Zhou and T. Liu are co-first authors.) (Corresponding authors: L. Shi and Q. Liu)

Z. Zhou is with School of Mathematics and Computer Sciences, Nanchang University, Nanchang, China.

L. Shi, T. Liu, B. Yu, Yanru Gong and Q. Liu are with School of Information Engineering, Nanchang University, Nanchang, China. (shiliu@ncu.edu.cn, liuqiegen@ncu.edu.cn)

Deep learning-based reconstruction models have gained increasing attention for their high computational speed [12] and robustness of parameter [13]. For example, post-processing methods for CT image domain reconstruction include FBP-ConvNet [14], dense deconvolution networks [11], and residual encoder-decoder convolutional neural networks [15]. Additionally, hybrid domain processing methods have been proposed to reconstruct high-quality images by learning from both the projection domain and the image domain [16], [17], such as hybrid domain neural network [18]. However, the performance of these methods for image reconstruction is still limited.

In recent years, diffusion models have been increasingly employed in SVCT reconstruction owing to their superior capabilities. Xia *et al.* [19] introduced a patch-based denoising probabilistic diffusion model to improve SVCT reconstruction performance and address large memory requirements. Additionally, Wu *et al.* [20] proposed an iteratively optimized data scoring model grounded in SGM to achieve high-quality CT reconstruction for ultra-sparse views. Guan *et al.* [21] introduced a score-based diffusion model that uses a multi-channel strategy in the projection domain to ensuring that the generated information closer to the original data, resulting in a more accurate SVCT reconstruction. Xia *et al.* [22] converted the denoising diffusion probability model into a parallel framework to improve the efficiency of the model, and applied it to the reconstruction of breast CT images in dual-domain sparse view. Yang *et al.* [23] introduced a dual-domain diffusion model for SVCT reconstruction, which includes a sinogram enhancement module and an image refinement module. However, the domain conversion process is limited by the sampling angle, which may lead to artifacts. Although diffusion models have achieved some success in SVCT reconstruction, they still have certain limitations in capturing finer information [24] and rely on large amounts of high-quality data for training [25].

The introduction of mask diffusion mitigates these limitations. Aversa *et al.* [26] used a layered diffusion model to generate synthetic segmentation masks for high-fidelity diffusion, reducing reliance on labeled data and preserving image detail and structure. Token *et al.* [27] used a denoising diffusion probability model to simultaneously generate images and masks, addressing data scarcity in satellite segmentation tasks while ensuring a wide diversity of samples. Konz *et al.* [28] applied mask diffusion to medical image segmentation, demonstrating its advantages when dealing with complex anatomical structures and reducing the reliance on large amounts of high-quality training data.

With the successful application of mask diffusion, it has been gradually introduced into the field of SVCT reconstruction. For example, Tan *et al.* [29] proposed a score-

based multiscale diffusion model. This method introduced a regular mask to reconstruct SVCT, which effectively improved the quality and performance of reconstructed images. However, this limits the network's ability to learn diverse data distributions, resulting in insufficient model generalization performance.

In order to solve the above issues, we introduce a **Sinogram Wavelet Random decomposition And Random mask diffusion Model (SWARM)**. The random mask strategy effectively expands the limited training sample space, enabling the model to learn a wider range of data distributions. This enhances its understanding of data uncertainty and improves generalization ability. By embedding random masks into sinograms, our method not only ensures that the model captures global information but also enhances its reliability in predicting unfamiliar data distributions. Subsequently, the sinogram wavelet random high-frequency refinement steps further improve the image quality. This strategy improves the model ability to capture details across different frequency bands by enhancing the feature representation, resulting in a reconstructed image with finer texture and clearer detail. By introducing data consistency constraints, the iterative reconstruction process of the two-stage model ensures global information consistency and enhances the accuracy of details such as texture, thereby improving the reliability of the reconstructed image.

The main contributions of this paper can be summarized as follows:

- **Multi-scale Joint Global-Detail Dual Diffusion.** We propose a combined global-detail training method that integrates a sinogram and wavelet high-frequency double diffusion model. By leveraging multi-scale analysis, this approach effectively captures both global information and detailed features in CT reconstruction tasks, thereby significantly enhancing models understanding of image structure.

- **Uncertainty Increasing of Random Mask Embedding in Sinogram Training.** We propose a training strategy for sinogram with random mask embedding. By randomly generating masks and embedding them into the sinogram, we increase sample diversity and expand the uncertainty of the feature space, thereby improving the model's generalization ability and enhancing the reliability of the reconstruction results.

- **Robust Feature Learning for Sinogram Random High-frequency.** The sinogram is decomposed using wavelet transform, and the high-frequency components are randomly selected as network inputs for training. This allows the model to focus on the details of specific frequencies, enhances the representation of spatial features in the data, and improves the model's adaptability to different frequency features, thereby enhancing its robustness.

In Section II, we provide a brief review of the relevant work. Section III outlines the theoretical approach and offers a detailed explanation of our proposed method. Section IV presents the experimental comparison results. Finally, in Section V, we discuss and conclude the methods presented.

## II. PRELIMINARY

### A. Sparse-view CT Image Reconstruction

Given an original image  $x$ , the image  $x$  is converted into full projection data through radon transformation, which is expressed as  $R(\theta, s) = \mathfrak{R}(x)(\theta, s)$ .  $R(\theta, s)$  denotes the outcome of the radon transformation at the position  $s$  for angle  $\theta$  along the projection direction, and  $\mathfrak{R}(x)(\theta, s)$  is the radon transform operator. The projection data obtained through scanning is a linear mapping of noise observation data to a set of measured values, expressed as:

$$y = Ax + \varepsilon, \quad (1)$$

where  $y$  represents the measured projected data,  $x$  represents the linear attenuation coefficient distribution of the internal structure of the object.  $A$  is the system matrix determined by the geometry of CT equipment and the scanning protocol used.  $\varepsilon$  is the system error noise during CT scanning.

SVCT reconstruction is a classical inverse problem [30]. Owing to the incompleteness in the data acquisition process, accurately reconstructing unknown images from limited measurements presents a significant challenge. The mapping from full projection data  $y$  to sparse-view data  $\hat{y}$  is a process of linear transformation. Specifically, for a linear mapping function  $f : \mathbb{R}^{m \times n} \rightarrow \mathbb{R}^{m \times n}$ , acting on  $y$  by the linear operator  $P(\wedge)$ , is obtained and expressed as:

$$\hat{y} = f(y) = P(\wedge)y. \quad (2)$$

Using the traditional FBP algorithm to reconstruct images directly from SVCT projection data can lead to severe fringe artifacts and blurred details. To improve the quality of reconstruction, it is usually necessary to incorporate prior information into the regularized objective function to address the following issues:

$$y^* = \arg \min_y \frac{1}{2} \|P(\wedge)y - \hat{y}\|_2^2 + \frac{\nu}{2} R(y), \quad (3)$$

where the first item is the data fidelity to ensure that the actual data obtained from under-sampling is aligned with the obtained measurement values. The second term is the regularization term, and the hyperparameter  $\nu$  used to balance the data fidelity term and the regularization term.

### B. Masked Diffusion

Diffusion models have achieved remarkable success in image, audio, and text fields with their high-quality data generation capability. In the forward process, the model gradually transforms the initial data distribution into a Gaussian distribution by progressively adding noise. In the reverse process, the model learns a reverse denoising process to gradually remove the noise, ultimately achieving accurate recovery of the original data. The research on diffusion model mainly focuses on the following aspects: denoising diffusion probabilistic models (DDPMs) [25], score-based generative models (SGMs) [31], and stochastic differential equations (SDEs) [32].

In recent years, masked diffusion has gained widespread application in image processing, particularly in tasks such as image synthesis [33]–[35], image editing [36]–[38], image

restoration [39], [40], image segmentation [41], [42] and image generation [29]. For example, in image synthesis, masks can be used to precisely control the position and shape of generated features, such as in wildfire generation [33]. In image recovery tasks, masks are used to recover occluded or damaged facial areas to achieve the effect of high-fidelity image recovery [39]. Meanwhile, in image segmentation tasks, labeled masks define the target regions, and diffusion models are used to optimize and refine the segmentation results [41]. In addition, in CT image reconstruction tasks, masks are also used in the reconstruction of multi-scale images [29]. These applications show that masks can effectively improve task performance in diffusion models.

Based on the successful application of masks in various image processing tasks, it still falls short when it comes to simulating missing or damaged data in projected data from real scans, we propose an innovative random mask diffusion method for sinogram. By applying random masks to sinograms, our method enables the model to learn from limited data, enhancing its generalization and robustness. Experimental results demonstrate effective improvements in image quality for SVCT reconstruction tasks with masked diffusion.

### III. METHOD

#### A. Motivation

In medical imaging, reconstructing high-quality images from sparse projections is vital for accurate diagnosis. When traditional deep models are trained on a closed dataset, satisfactory reconstruction results are achieved within similar data distributions. However, these models tend to decrease diagnostic accuracy and reliability when applied to unfamiliar data, which poses potential clinical risks [43].

Embedding a random mask in a sinogram can enhance the model's ability to deal with data uncertainty, bolstering its reliability with respect to unfamiliar data distributions. As shown in Fig. 1(a), data distributions with the same or similar data produce relatively uniform results. As shown in Fig. 1(b), a more diverse sample of uncertain data is introduced by embedding random masks in Fig. 1(c), making the data distribution more extensive.

We provide a theoretical guarantee for the proposed sinogram based random mask embedding strategy and prove the validity of random mask.

**Proposition 3.1:** The incorporation of random masks into a finite sinogram sample set  $x = \{x_1, x_2, \dots, x_n\}$ , serves to augment the variance of the data distribution.

**Proof:** Let  $x_M$  represent the sinogram after random masking  $m$ . The perturbed data  $\tilde{x}$  can be expressed as the sum of the sinogram and its corresponding mask, such that  $\tilde{x} = x + x_M$ . The mean of the perturbed data  $\tilde{x}$ , denoted as  $\tilde{\mu}$ , can be formulated as follows:

$$\tilde{\mu} = \frac{1}{n} \sum_{i=1}^n (x_i + x_{M_i}), \quad (4)$$

The variance of the data after the application of masking can be represented as follows:

$$\sigma^2(\tilde{x}) = \frac{1}{n} \sum_{i=1}^n ((x_i - \mu) + (x_{M_i} - \mu_M))^2, \quad (5)$$

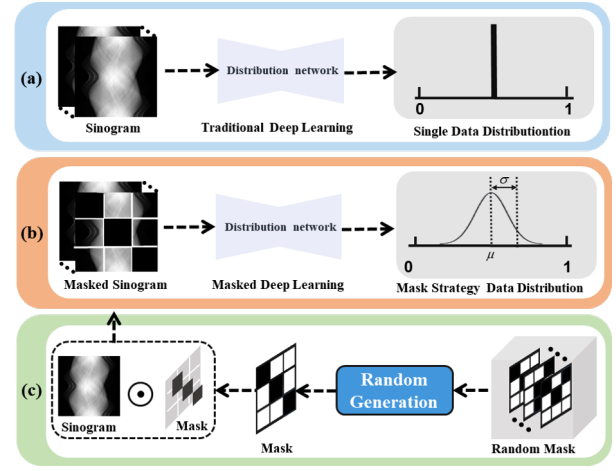


Fig. 1: Different training strategies and influence of sinogram in deep learning. (a) Distribution of training data in a closed data space; (b) The distribution of the data obtained through the mask extension method in the extended data space; (c) The generation process of the random mask and how it is embedded in the data.

where  $\sigma^2(\tilde{x})$  is the variance of  $\tilde{x}$ ,  $\mu$  and  $\mu_M$  represent the mean of  $x$  and  $x_M$ , respectively. Depending on the properties of expectation and variance, Eq. (5) can be rewritten as:

$$\sigma^2(\tilde{x}) = \sigma^2(x) + \frac{1}{n} \sum_{i=1}^n 2(x_i - \mu)(x_{M_i} - \mu_M) + \frac{1}{n} \sum_{i=1}^n (x_{M_i} - \mu_M)^2, \quad (6)$$

where  $\sigma^2(x)$  is the variance of  $x$ . For an arbitrary random mask  $m_i$ , we have  $x_{M_i} = x_i \cdot m_i$  and  $\mu_M = \frac{1}{n} \sum_{j=1}^n x_j \cdot m_j$ . Extracting the cross terms of Eq. (6), then

$$\mathcal{F} = \frac{1}{n} \sum_{i=1}^n 2(x_i - \mu)(x_{M_i} - \mu_M) = \frac{1}{n} \sum_{i=1}^n 2(x_i - \mu)(x_i m_i - \frac{1}{n} \sum_{j=1}^n x_j m_j). \quad (7)$$

$\mathcal{F}$  can be decomposed into the sum of two terms, i.e.,  $\mathcal{F} = \mathcal{F}_1 - \mathcal{F}_2 = \frac{1}{n} \sum_{i=1}^n 2(x_i - \mu)(x_i m_i) - \frac{1}{n} \sum_{i=1}^n 2(x_i - \mu)(\frac{1}{n} \sum_{j=1}^n x_j m_j)$ . It implies that  $\mathbb{E}[m_i] = \frac{a+b}{2}$  since  $m_i \sim U(a, b)$ . Let  $\mathbb{E}[\cdot]$  stands for expectation. Then we have  $\mathbb{E}[\mathcal{F}_1] = \frac{1}{n} \sum_{i=1}^n 2(x_i - \mu)x_i \mathbb{E}[m_i] = \frac{a+b}{2} \cdot \frac{2}{n} \sum_{i=1}^n (x_i - \mu)x_i = 0$  since  $\sum_{i=1}^n (x_i - \mu)x_i = \sigma^2(x)$  is the variance term, the expectation is 0. Moreover,  $\mathbb{E}[\mathcal{F}_2] = -\frac{2}{n^2} \sum_{i=1}^n \sum_{j=1}^n (x_i - \mu) \cdot x_j \cdot \frac{a+b}{2} = 0$  since  $\sum_{i=1}^n (x_i - \mu) = 0$ . Hence,  $\mathbb{E}[\mathcal{F}] = 0$ .

Since  $\mathbb{E}[\frac{1}{n} \sum_{i=1}^n (x_{M_i} - \mu_M)^2] \geq 0$ , it means that  $\mathbb{E}[\sigma^2(\tilde{x})] \geq \sigma^2(x)$ . Therefore, the random mask strategy we introduce to the data set is effective.  $\square$

The high-frequency components extracted by wavelet transform are essential for capturing complex texture details in images. The method of randomly embedding high-frequency components can enhance the ability of the model to recognize and capture image details, so as to improve the performance of the model in the reconstruction of detail information. This method helps to improve the stability and accuracy of the model, ensuring that the denoised image can truly reflect the fine features of the original scene.

Through two-stage iterative optimization process, the algorithm ensures global consistency in images while generating high-quality ones with rich texture and clear details. This

method effectively enhances the accuracy and robustness of the reconstruction results, ensuring the fidelity and precision of the sinogram, and achieving more accurate and reliable image reconstruction.

## B. Training Process in Sinogram Wavelet Domain

1) *Random Mask Strategy in Sinogram Domain*: In the prior learning phase based on the projection domain, we propose a training strategy that involves embedding random masks into sinograms. By applying random masks to the sinograms, this method introduces random perturbations within the limited data sample space, effectively increasing the diversity of the feature space and enhancing the model focus on a wider range of data distributions, thereby improving its generalization ability as well as the reliability and accuracy of the reconstructed results.

According to the physical characteristics of projection data acquisition, we have specially designed a random mask strategy to address issues such as missing scanning angles, detector ray damage, and the random loss of some projection data. By applying randomly generated masks to the projection data, we introduce uncertainty to enhance model robustness. Specifically, given full-view projection data  $y$  and the random mask operator  $\hat{m}$ , the masked full-view projection data can be expressed as:

$$\tilde{Y}_s = y \odot \hat{m}, \quad (8)$$

where  $\tilde{Y}_s$  indicates the projected data with the mask.

The mask strategy as follows: Given arbitrary mask type, the seed set  $M = \{M_1, M_2, M_3\}$ . The type symbol  $S$  is generated randomly from  $\{1, 2, \dots, n\}$ . Randomly generated mask type symbol is marked as  $M_s$ . The set of random mask locations under  $M_s$  is marked as  $\hat{S}$ . The randomly mask generated as follows:

$$\hat{m}_{i,j} = \begin{cases} 0, & (i,j) \in \hat{S}, \\ 1, & (i,j) \notin \hat{S}, \end{cases} \quad (9)$$

where  $s \sim \text{Uniform}\{1, 2, \dots, n\}$ ,  $\hat{m}$  is the mask generated by random rules.

2) *Random High-frequency in Sinogram Wavelet Domain*: Prior learning in the projection domain focuses more on global information and tends to ignore the details. To improve the detail quality of reconstructed images, we propose a sinogram wavelet-based random high-frequency diffusion strategy. By performing wavelet decomposition of the sinogram and randomly selecting high-frequency components as network inputs for training, this approach enables the model to focus on specific frequency details. Additionally, the introduction of random high-frequency components enhances feature representation in the data space. This improvement bolsters the model's adaptability to a variety of frequency features and significantly aids in the recovery of fine textures and other detailed characteristics in the reconstructed images.

Specifically, decomposing the sinogram into four sub-images using Discrete Wavelet Transform (DWT): the low-frequency approximation component (LL) and the high-frequency detail components (LH, HL, HH). This process can

be expressed as:

$$H : y \rightarrow \{h_{LL}(y), h_{LH}(y), h_{HL}(y), h_{HH}(y)\}, \quad (10)$$

where  $H$  represents the wavelet transform,  $h_{LL}$  represents the low-frequency component after the transformation,  $h_{LH}$ ,  $h_{HL}$  and  $h_{HH}$  correspond to the high-frequency detail components in the vertical, horizontal and diagonal directions respectively. Let the three high-frequency components be denoted as  $Y_h = \{h_{LH}(y), h_{HL}(y), h_{HH}(y)\}$ . By randomly selecting a high-frequency sub-image  $\tilde{Y}_h$  from the wavelet domain for training, the ability of the network to learn texture details.

3) *Forward Diffusion Process Based on SDEs*: The two-stage training is carried out through a score generation model based on stochastic differential equations (SDEs) to obtain the Sinogram Random Mask model (SRM) and Sinogram wavelet random High-frequency Decomposition model (SHD), respectively. In the training stage, the model mainly includes two processes: the forward process and the backward process. As shown in Fig. 2(a) and Fig. 2(b), the forward process of the projection domain and the wavelet domain during the training phase is illustrated in detail. In this process, the forward stochastic differential equation (SDE) progressively transforms a complex data distribution into a tractable Gaussian distribution by gradually adding noise.

Given a diffusion process  $\{x(t)\}_{t=0}^T$ , represented by a continuous time variable  $t \in [0, T]$ , such that  $x(t) \sim p_t$ , where the sample image data is independently and identically distributed. The forward SDE process is expressed as follows [30]:

$$dx = f(x, t)dt + g(t)dw, \quad (11)$$

where  $f(x, t) : \mathbb{R}^N \rightarrow \mathbb{R}^N$  is a vector-valued function and  $\mathbb{R} \rightarrow \mathbb{R}$  is a scalar function about  $x(t)$ , which are called drift coefficient and diffusion coefficient respectively.  $N$  indicates the dimension of the image data in the projection domain.  $w \in \mathbb{R}^N$  induces the standard Brownian motion.

Variance explosion SDE (VE-SDE) is obtained by applying  $f(x, t) = 0$ ,  $g(t) = \sqrt{d[\sigma^2(t)]/dt}$  in order to improve the capability. In this case, the two-stage VE-SDE is represented as follows:

$$d\tilde{Y}_s = \sqrt{d[\sigma^2(t)]/dt}dw, \quad (12)$$

$$d\tilde{Y}_h = \sqrt{d[\sigma^2(t)]/dt}dw, \quad (13)$$

where  $\sigma(t) > 0$  represents a monotonically increasing function and signifies the time-varying escalating scale function for noise.

During the prior learning stage in the projection domain, we progressively introduce Gaussian noise into  $\tilde{Y}_s$ . The network  $\mathbf{s}_{\theta_s}(\tilde{Y}_s(t), t)$  is optimized by tuning the parameter  $\theta_s$  to achieve optimal performance. The specific optimization objective function is given by:

$$\theta_s^* = \arg \min_{\theta_s} \mathbb{E}_t \{ \lambda_t \mathbb{E}_{\tilde{Y}_s(0)} \mathbb{E}_{\tilde{Y}_s(t)|\tilde{Y}_s(0)} [\| \mathbf{s}_{\theta_s}(\tilde{Y}_s(t), t) - \nabla_{\tilde{Y}_s(t)} \log p_{0t}(\tilde{Y}_s(t)|\tilde{Y}_s(0)) \|_2^2] \}, \quad (14)$$

where  $\lambda_t$  is a positive function,  $\log p_{0t}(\tilde{Y}_s(t)|\tilde{Y}_s(0))$  is the gaussian perturbation kernel centered at  $\tilde{Y}_s(0)$ . Once the

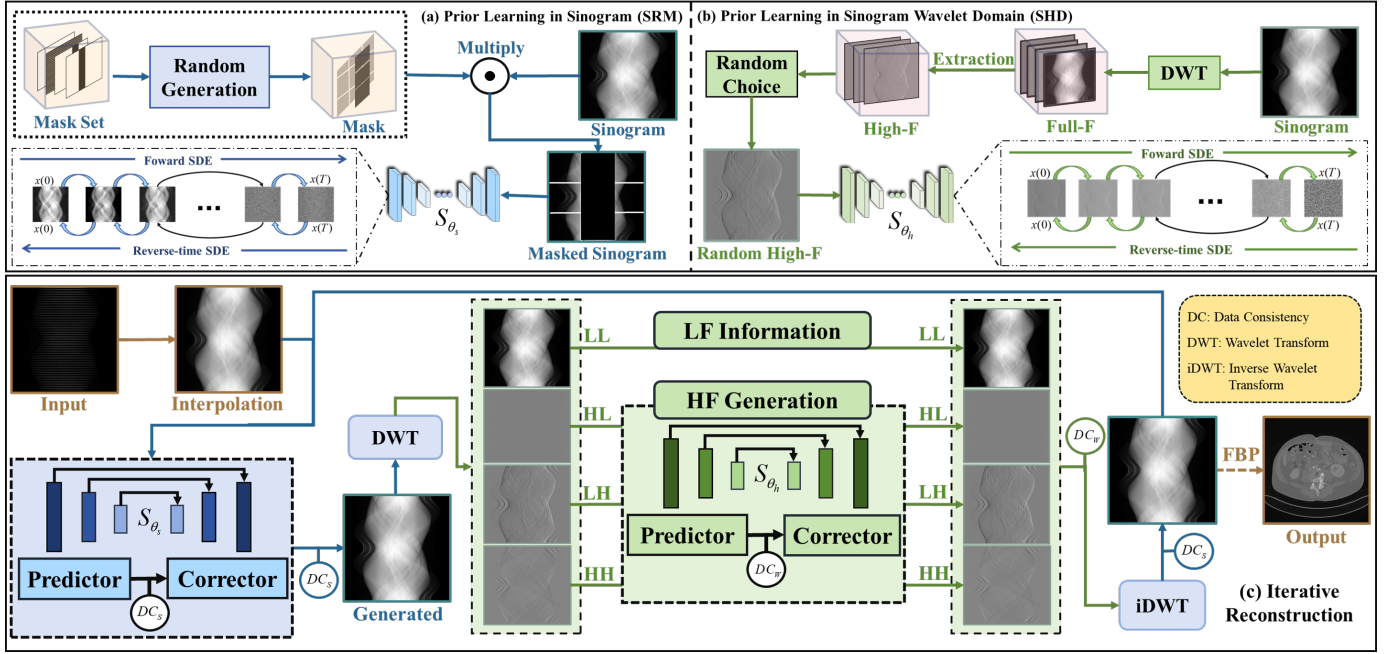


Fig. 2: Training stage: (a) A model training based on random masks in sinogram. (b) A model training for high-frequency random decomposition of wavelet based on sinogram. Iteration reconstruction stage: (c) The proposed SWARM method is used to reconstruct the sparse-view CT projection domain. “LF”: Low-frequency. “HF”: High-frequency.

network satisfies  $\tilde{Y}_s(t) \simeq \nabla_{\tilde{Y}_s(t)} \log p_{0t}$  and  $\nabla_{\tilde{Y}_h(t)} \log p_{0t}$  will be known for all  $t$  by solving  $\nabla_{\tilde{Y}_s(t)} \log p_{0t}$ .

The prior learning stage for random wavelet high-frequency components involves training the high-frequency components through the neural network  $\mathbf{s}_{\theta_h}(\tilde{Y}_h(t), t)$ . Gaussian noise is gradually introduced into randomly selected high-frequency wavelet components to optimize the network parameters. The optimization objective function of this process is as follows:

$$\theta_h^* = \arg \min_{\theta_h} \mathbb{E}_t \{ \lambda_t \mathbb{E}_{\tilde{Y}_h(0)} \mathbb{E}_{\tilde{Y}_h(t) | \tilde{Y}_h(0)} [ \| \mathbf{s}_{\theta_h}(\tilde{Y}_h(t), t) - \nabla_{\tilde{Y}_h(t)} \log p_{0t}(\tilde{Y}_h(t) | \tilde{Y}_h(0)) \|_2^2 ] \}. \quad (15)$$

Alg. 1 provides a detailed description of SRM and SHD in the training process.

### Algorithm 1

#### SRM Training process

- 1: Load projected data  $y$  from the training set;
- 2: Randomly generated a discrete random mask  $\hat{m}$ ;
- 3: Generate a masked sinogram:  $\tilde{Y}_s = y \odot \hat{m}$ ;
- 4: Trained with SRM;
- 5: Output  $\mathbf{s}_{\theta_s}(\tilde{Y}_s, t)$ .

#### SHD Training process

- 1: Load projected data  $y$  from the training set;
- 2: Wavelet transform:  
 $H : y \rightarrow \{h_{LL}(y), h_{LH}(y), h_{HL}(y), h_{HH}(y)\}$ ;
- 3: Random selection of high-frequency components:  
 $\tilde{Y}_h \leftarrow \{h_{LH}(y), h_{HL}(y), h_{HH}(y)\}$ ;
- 4: Trained with SHD;
- 5: Output  $\mathbf{s}_{\theta_h}(\tilde{Y}_h, t)$ .

To sum up,  $\mathbf{s}_{\theta_s}(\tilde{Y}_s(t), t)$  and  $\mathbf{s}_{\theta_h}(\tilde{Y}_h(t), t)$  can accurately learn the data distribution of real images in the projection domain and the high-frequency data distribution of sinogram

wavelet. This approach not only enhances the model ability to recognize the global structure of the image but also improves its sensitivity to details such as texture. With this dual-model strategy, the model is further encouraged to learn and approximate the underlying probability distribution of the data.

### C. Cascade Reconstruction of Sinogram and Wavelet

The image generation process in iterative reconstruction is essentially the inverse problem of SDEs, specifically a reverse diffusion process. By utilizing prior knowledge from the SRM and SHD, we ensure that the reconstruction stage generates comprehensive global information and finer details. Combined with data consistency constraints, SDEs employ a predictor-corrector (PC) sampler to efficiently generate high-quality images. This process can be represented by the following reverse-time SDE:

$$d\hat{y} = [f(\hat{y}, t) - g^2(t) \nabla_{\hat{y}} \log p_t(\hat{y})] dt + g(t) d\bar{w}, \quad (16)$$

where  $dt$  is an infinitesimal negative time step,  $\bar{w}$  is a standard Brownian motion with time flows backwards from  $T \rightarrow 0$ .  $\nabla_{\hat{y}} \log p_t(\hat{y})$  is the score for each marginal distribution,  $\hat{y} = \{\hat{y}_s, \hat{y}_h\}$  includes the sinogram and its wavelet high-frequency regions.  $\nabla_{\hat{y}} \log p_t(\hat{y})$  can be estimated by training a time-dependent scoring network  $\mathbf{s}_{\theta}(\hat{y}, t) = \{\mathbf{s}_{\theta}(\hat{y}_s, t), \mathbf{s}_{\theta}(\hat{y}_h, t)\}$  to satisfy  $\mathbf{s}_{\theta}(\hat{y}, t) \simeq \nabla_{\hat{y}} \log p_t(\hat{y})$ . The score function  $\theta^*$  can be estimated by network training in the learning stage of prior information. The scoring estimator  $\mathbf{s}_{\theta}(\hat{y}_{s,t}, t)$  can replace Eq. (16) to approximate the solution of the score function:

$$d\hat{y} = [f(\hat{y}, t) - g^2(t) \mathbf{s}_{\theta}(\hat{y}, t)] dt + g(t) d\bar{w}. \quad (17)$$

In the joint iterative reconstruction stage, by introducing regularized prior information, the model is guided to gradually integrate the global consistency in the projection domain with

the detailed features in the high-frequency components of the wavelet. The overall optimization objectives are as follows:

$$\{\hat{y}_s^*, \hat{y}_h^*\} = \arg \min_{\hat{y}_s, \hat{y}_h} \|P(\wedge)y - \hat{y}_s^*\|_2^2 + \beta \|\tilde{H}_h[P(\wedge)y - \hat{y}_h]\|_2^2 + \nu_s R_s(\hat{y}_s) + \nu_h R_h(\hat{y}_h), \quad (18)$$

where  $\hat{y}_s$  and  $\hat{y}_h$  represent the projection domain and the wavelet domain data in the reconstruction stage, respectively.  $\tilde{H}_h[\cdot]$  represents extracting the high-frequency components of the wavelet domain from the sinogram. The hyperparameters  $\nu_s$  and  $\nu_h$  are used to balance data consistency and regularized priors. High-frequency information extraction is expressed as follows:

$$\tilde{H}_h[\cdot] = \tilde{H}[\cdot]/\tilde{H}_l[\cdot], \quad (19)$$

where  $\tilde{H}[\cdot]$  represents the full-frequency information,  $\tilde{H}_l[\cdot]$  represents the low-frequency component and  $\tilde{H}_h[\cdot]$  represents the high-frequency component.

We optimize the two-stage process through successive iterations of SRM and SHD. Specifically, SRM is optimized using a sinogram-based score model, while SHD is optimized by enhancing the details of the high-frequency components in the wavelet domain. This approach facilitates the transition from global consistency to fine details. The process can be formalized into the following two steps:

$$\hat{y}_s^{t-1} = \arg \min_{\hat{y}_s} \|P(\wedge)y - \hat{y}_s\|_2^2 + \nu_s R_s(\hat{y}_s^t), \quad (20)$$

$$\hat{y}_{h,i}^{t-1} = \arg \min_{\hat{y}_{h,i}} \|\tilde{H}_h(P(\wedge)y) - \hat{y}_{h,i}\|_2^2 + \nu_h R_h(\tilde{H}_h[\hat{y}_s^{t-1}]). \quad (21)$$

**1) Sinogram Generation:** The sinogram generation stage, as the first subproblem, is designed to enhance global information to ensure data consistency and integrity. This stage can be broken down into the following two subproblems:

$$\hat{y}_s^{t-\frac{1}{2}} = \arg \min_{\hat{y}_s} \|\hat{y}_s - P(\wedge)y\|_2^2 + \mu_s \|\hat{y}_h^t - \tilde{H}_h[\hat{y}_s]\|_2^2, \quad (22)$$

$$\hat{y}_s^{t-1} = \arg \min_{\hat{y}_s} \|\hat{y}_s - \hat{y}_s^{t-\frac{1}{2}}\|_2^2 + \nu_s R_s(\hat{y}_s). \quad (23)$$

Eq. (22) can be considered a data consistency term for the sinogram, which can be simplified to the following equation by ensuring the alignment between the generated data and the original data:

$$\hat{y}_s^{t-\frac{1}{2}} = (1 - P(\wedge))\hat{y}_s^{t-\frac{1}{2}} + P(\wedge)y. \quad (24)$$

The predictor serves as a variance explosion (VE) SDE solver to generate an estimate for the next reconstruction iteration, which is solved numerically through backdiffusion. Using the trained model  $\mathbf{s}_{\theta_s}$  for the reverse SDE generates samples, and the discretization of the predictor is formulated as follows:

$$\hat{y}_s^{t-1} = \hat{y}_s^{t-\frac{1}{2}} + (\delta_t^2 - \delta_{t-1}^2)\mathbf{s}_{\theta_s}(\hat{y}_s^{t-\frac{1}{2}}, t) + \sqrt{\delta_t^2 - \delta_{t-1}^2}z, \quad (25)$$

where  $\delta_t$  represents a monotonically increasing function with respect to time  $t$ .  $z \sim \mathcal{N}(0, 1)$  is a Gaussian distribution following random noise. The corrector uses Langevin dynamics to convert the initial sample  $\hat{y}_s(0)$  to the final sample  $\hat{y}_s(t)$ , the steps to implement the ‘‘corrector’’ are as follows:

$$\hat{y}_s^{t-1} = \hat{y}_s^{t-1} + \varepsilon_{t-1}\mathbf{s}_{\theta_s}(\hat{y}_s^{t-1}, t) + \sqrt{2\varepsilon_{t-1}}z, \quad (26)$$

where  $\varepsilon > 0$  is the step size and the above equation is repeated for  $t = T - 1, \dots, 0$ . The solution is optimized by alternating iterations of the ‘‘predictor’’ and ‘‘corrector’’ steps above to achieve convergence.

**2) High-frequency generation in wavelet domain:** Upon completion of the reconstruction in the projection domain during the first stage, the sinogram is subsequently transformed into the wavelet domain. In this domain, three high-frequency components are extracted, whereas the low-frequency component is preserved. The process can be described as follows:

$$\begin{aligned} \hat{y}_h^{t-\frac{1}{2}} &= \tilde{H}[\hat{y}_s^{t-1}]/\tilde{H}_l[\hat{y}_s^{t-1}] = \tilde{H}_h[\hat{y}_s^{t-1}] \\ &= \{\hat{y}_{LH}^{t-\frac{1}{2}}, \hat{y}_{HL}^{t-\frac{1}{2}}, \hat{y}_{HH}^{t-\frac{1}{2}}\}. \end{aligned} \quad (27)$$

Building on the approach used for the subproblem in the projection domain during the first stage, the high-frequency components extracted from the wavelet domain are employed to optimize the score-based generation model. This optimization refines intricate details, such as complex textures. The updated objective function is expressed as follows:

$$\hat{y}_{h,i}^{t-\frac{1}{2}} = \arg \min_{\hat{y}_{h,i}} \|\hat{y}_{h,i} - \tilde{H}_h[P(\wedge)y]\|_2^2 + \mu_h \|\hat{y}_s^{t-1} - \hat{y}_s\|_2^2, \quad (28)$$

$$\hat{y}_{h,i}^{t-1} = \arg \min_{\hat{y}_{h,i}} \|\hat{y}_{h,i} - \hat{y}_{h,i}^{t-\frac{1}{2}}\|_2^2 + \nu_{h,i} R_h(\hat{y}_{h,i}), \quad (29)$$

where  $\hat{y}_{h,i}$  represents the  $i$ -th high-frequency component and  $i = 0, 1, 2$ .

According to the data consistency of the high-frequency components in the wavelet domain, to ensure the reliability of the data:

$$\hat{y}_{h,i}^{t-\frac{1}{2}} = \tilde{H}_h[(1 - P(\wedge))\hat{y}_s^{t-\frac{1}{2}} + P(\wedge)y]. \quad (30)$$

At this stage, the same ‘‘predictor’’ and ‘‘corrector’’ steps of the VE-SDE diffusion model are applied to the high-frequency components of each channel. Specifically, the ‘‘predictor’’ step uses the trained  $\mathbf{s}_{\theta_h}$  network for reconstruction, as follows:

$$\hat{y}_{h,i}^{t-1} = \hat{y}_{h,i}^{t-\frac{1}{2}} + (\delta_t^2 - \delta_{t-1}^2)\mathbf{s}_{\theta_h}(\hat{y}_{h,i}^{t-\frac{1}{2}}, t) + \sqrt{\delta_t^2 - \delta_{t-1}^2}z. \quad (31)$$

Then, perform the ‘‘corrector’’ step as well, as follows:

$$\hat{y}_{h,i}^{t-1} = \hat{y}_{h,i}^{t-1} + \varepsilon_{t-1}\mathbf{s}_{\theta_h}(\hat{y}_{h,i}^{t-1}, t) + \sqrt{2\varepsilon_{t-1}}z. \quad (32)$$

**3) Domain transform stage:** Ultimately, the process integrates the retained low-frequency information with the optimized high-frequency components. This combined data is then transformed back to the projection domain via wavelet inversion, as detailed below:

$$\hat{y} = \tilde{H}^T[\tilde{H}_l[\hat{y}_s], \tilde{H}_h[\hat{y}_s]]. \quad (33)$$

Upon completion of the iteration, the final reconstructed image is generated by applying the Filtered Back Projection (FBP) algorithm for back projection. The expression for this process is as follows:

$$\tilde{x} = FBP(\hat{y}). \quad (34)$$

In summary, the iterative reconstruction phase of SWARM is illustrated in Fig. 2(c). The models are trained by embedding

random masks in the sinogram and employing random high-frequency strategies in the sinogram wavelet domain to capture the prior distributions of global information and detailed features. During reconstruction, the numerical SDE solver and Langevin dynamics are iteratively updated to obtain high-quality full-view projection data. The detailed process of the reconstruction stage is shown in Alg. 2.

---

**Algorithm 2**


---

**SWARM Iterative Reconstruction**


---

**Setting:**  $\mathbf{s}_{\theta_s}, \mathbf{s}_{\theta_h}, \sigma, \varepsilon$ ;

- 1:  $\hat{Y}_s^T \sim \mathcal{N}(0, \sigma_{max}^2), \hat{Y}_h^T \sim \mathcal{N}(0, \sigma_{max}^2)$ ;
  - 2: For  $t = T - 1$  to 0 do:
  - 3:  $\hat{Y}_s^{t-\frac{1}{2}} \leftarrow \text{predictor}(\hat{Y}_s^t, \sigma_{t-1}, \sigma_t, \mathbf{s}_{\theta_s})$ ;
  - 4: Update  $\hat{Y}_s^{t-\frac{1}{2}}$  by data consistency with Eq. (24);
  - 5:  $\hat{Y}_s^{t-1} \leftarrow \text{corrector}(\hat{Y}_s^{t-\frac{1}{2}}, \sigma_{t-1}, \varepsilon_{t-1}, \mathbf{s}_{\theta_s})$ ;
  - 6: Update  $\hat{Y}_s^{t-1}$  by data consistency with Eq. (24);
  - 7: For  $i = 1$  to 3 do:
  - 8:  $\hat{Y}_{h,i}^{t-\frac{1}{2}} \leftarrow \text{predictor}(\hat{Y}_{h,i}^t, \sigma_{t-1}, \sigma_t, \mathbf{s}_{\theta_h})$ ;
  - 9: Update  $\hat{Y}_{h,i}^{t-\frac{1}{2}}$  by data consistency with Eq. (30);
  - 10:  $\hat{Y}_{h,i}^{t-1} \leftarrow \text{corrector}(\hat{Y}_{h,i}^{t-\frac{1}{2}}, \sigma_{t-1}, \varepsilon_{t-1}, \mathbf{s}_{\theta_h})$ ;
  - 11: Update  $\hat{Y}_{h,i}^{t-1}$  by data consistency with Eq. (30);
  - 12: End for
  - 13: End for
  - 14: Obtain the final image  $\tilde{x}$ ;
  - 15: Return  $\tilde{x}$ .
- 

## IV. EXPERIMENT

### A. Data Specification

1) *AAPM Challenge Data*: The dataset used for training and testing is part of the AAPM Low-Dose Challenge [44] provided by the Mayo Clinic. It consists of 5,388 CT slices from 10 patients. In this study, 4,742 slices from 9 patients were used for training, while 12 slices from the remaining patient were used for testing. Each slice is 1 mm thick. To evaluate the performance of the proposed method with different sparse views, CT images were reconstructed using 30, 60, 90 and 120 projections, and both qualitative and quantitative analyses were performed. Reference images are generated from 720 projection views using the FBP algorithm. For the fan-beam CT reconstruction task, ray-driven algorithms [45], [46] were employed to simulate the generation of projection data. The distance from the center of rotation to the source and detector is set at 40 cm and 40 cm, respectively. The detector is 41.3 cm wide, has 720 detector elements, and a total of 720 projection views are evenly distributed.

2) *CIRS Phantom Data*: We use a dataset of high-quality CT scans to further analyze the performance of the proposed method, each with dimensions of  $512 \times 512 \times 100$  voxels, and a voxel dimension of  $0.78 \times 0.78 \times 0.625$  mm<sup>3</sup>. The data set was collected using the GE Discovery HD750 CT scanner combined with a bionic model provided by CIRS. The vacuum tube current is set to 600 mAs, the source-wheelbase separation of the CT system is 573mm, and the source-detector distance

is 1010 mm. To evaluate the efficacy of the reconstruction algorithms across different sparse-view sampling scenarios, CT images were reconstructed using 30, 60, 90 and 120 projection, the reconstruction results underwent both qualitative and quantitative analysis.

### B. Implementation Details

In the experimental part of this study, we use Adam algorithm to train the model, and the learning rate is set to  $10^{-3}$ . At the same time, use the Kaiming initialization to initialize the weights of the model. Three kinds of simulation masks are designed in this method. The first simulates the 10, 20, 30, 60, 90, 120, 180, and 720 projection angles of the sparse view mask. The second is three randomly positioned circle masks with a radius of 48 pixels; The third is a mask one-fifth of the width of the original image. At the same time, use the Kaiming initialization to initialize the weights of the model. The method is implemented in Python using Operator Discretization Library (ODL) [47] and PyTorch on a personal workstation with a GPU card (Tesla V100-PCIE-16 GB). In the reconstruction process, set the iteration parameter of  $N < 1200$ . Our source code is publicly available on GitHub and can be accessed via the following link: <https://github.com/yqx7150/SWARM>. To evaluate the performance quantitatively, peak signal-to-noise ratio (PSNR), structural similarity index (SSIM) and mean square error (MSE) were used.

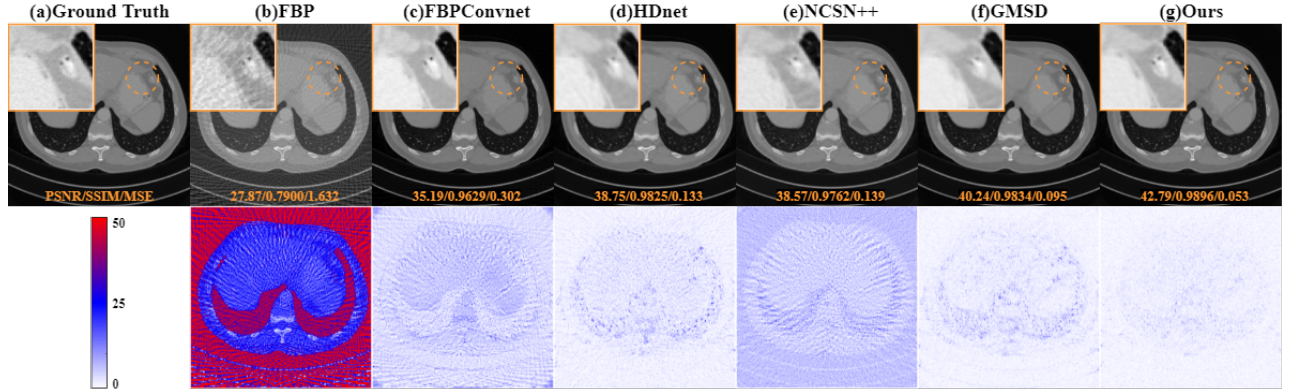
### C. Reconstruction Experiments

1) *AAPM Reconstruction Results*: In order to assess the effectiveness of the proposed algorithm, we will evaluate the performance and compare some representative methods including FBP [48], FBPCnvNet [14], HDNet [18], NCSN++ [32], GMSD [21]. Sparse-view CT reconstructions were conducted using 30, 60, 90 and 120 projections, respectively. Table I presents the PSNR, SSIM, and MSE values for the reconstruction results of the AAPM challenge dataset. The best values for reconstructed images with different projection views are highlighted in bold. SWARM demonstrates superior performance over other reconstruction techniques in terms of mean values for the AAPM test data. In contrast, FBP and HDNet exhibit inferior numerical performance for CT reconstruction under sparse-view conditions. Furthermore, SWARM shows significant advantages over existing technologies.

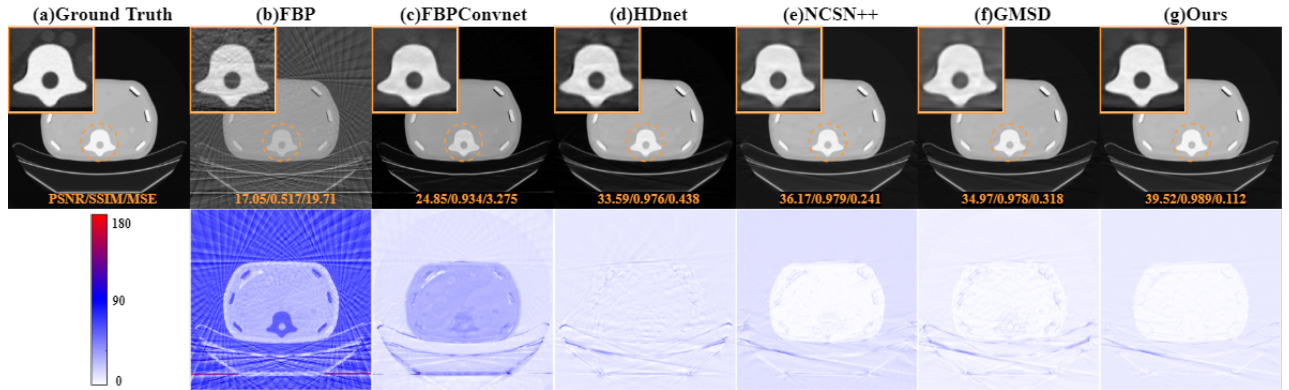
Fig. 3 shows the visual reconstruction results of the AAPM test dataset. The traditional FBP reconstruction exhibits poor image quality, characterized by blurred details and significant edge artifacts. Although FBPCnvNet has shown some improvements, it still suffers from edge blurring and a loss of finer details. The complex dual-domain iterative model HDNet, while effective in certain aspects, leads to information loss due to excessive smoothing. Additionally, NCSN++ and GMSD reconstruction also results in a noticeable loss of texture details and the presence of edge artifacts after iterative processing. In contrast, SWARM not only effectively eliminates edge artifacts but also preserves more structural and textural details, and the reconstruction results are closer to groundtruth.

**TABLE I:** Reconstruction PSNR/SSIM/MSE( $10^{-3}$ ) of AAPM Challenge Data Using Different Methods at 30, 60, 90, 120 Views.

Views	FBP [48]	FBPConvNet [14]	HDNet [18]	NCSN++ [32]	GMSD [21]	SWARM
30	19.16/0.4596/12.561	29.76/0.9403/1.175	28.30/0.9347/2.070	32.66/0.9445/0.596	31.11/0.7888/0.849	<b>34.38/0.9585/0.415</b>
60	23.28/0.5957/4.815	34.23/0.9564/0.402	35.28/0.9706/0.345	36.97/0.9723/0.232	36.29/0.8445/0.276	<b>38.65/0.9779/0.163</b>
90	26.32/0.7088/2.388	36.25/0.9611/0.260	38.45/0.9809/0.164	39.64/0.9820/0.116	39.22/0.8745/0.127	<b>41.76/0.9877/0.070</b>
120	28.50/0.7961/1.447	38.03/0.9692/0.161	39.21/0.9851/0.151	40.82/0.9854/0.093	40.53/0.9060/0.097	<b>42.96/0.9901/0.053</b>

**Fig. 3:** Reconstruction images from 120 views using different methods with AAPM challenge data. (a) The reference image versus the images reconstructed by (b) FBP, (c) FBPConvNet, (d) HDNet, (e) NCSN++, (f) GMSD and (g) SWARM. The display window is [0, 50] HU. The second line is the residual between the reference image and the reconstructed image.**TABLE II:** Reconstruction PSNR/SSIM/MSE( $10^{-3}$ ) of CIRS Phantom Data Using Different Methods at 30, 60, 90, 120 Views.

Views	FBP [48]	FBPConvNet [14]	HDNet [18]	NCSN++ [32]	GMSD [21]	SWARM
30	12.67/0.4002/54.086	23.93/0.8850/4.052	27.27/0.9222/1.898	27.30/0.9287/1.923	27.54/0.7914/1.785	<b>30.58/0.9618/0.899</b>
60	17.15/0.5057/19.294	24.25/0.9308/3.762	32.53/0.9750/0.562	34.88/0.9765/0.329	33.07/0.8675/0.499	<b>38.45/0.9886/0.144</b>
90	21.78/0.6215/6.636	29.60/0.9320/1.102	37.21/0.9881/0.193	40.03/0.9879/0.101	37.75/0.8913/0.170	<b>44.70/0.9957/0.035</b>
120	25.08/0.6940/3.102	31.19/0.9444/0.764	40.20/0.9916/0.970	42.73/0.9920/0.054	39.86/0.9148/0.104	<b>46.68/0.9968/0.022</b>

**Fig. 4:** Reconstruction images from 60 views using different methods with CIRS phantom data. (a) The reference image versus the images reconstructed by (b) FBP, (c) FBPConvNet, (d) HDNet, (e) NCSN++, (f) GMSD and (g) SWARM. The display window is [0,180] HU. The second line is the residual between the reference image and the reconstructed image.

**2) CIRS Phantom Reconstruction Results:** To further evaluate the generalization and robustness of the proposed unsupervised learning method, prior knowledge was learned from the AAPM challenge dataset, and the model performance was assessed using CIRS simulated test data. Table II show that SWARM significantly outperforms the other approaches in terms of quantitative metrics. The image quality of FBP and FBPConvNet on the CIRS phantom dataset is notably inferior, indicating considerable loss of image details. Although the quantitative metrics of HDNet, NCSN++ and GMSD remain relatively stable, their reconstruction performance still shows a noticeable decline. In contrast, SWARM got the best results, demonstrating its strong generalization and robustness.

As shown in Fig. 4, our method achieves excellent visual

results. The images reconstructed using FBP exhibit significant streak artifacts and detail loss. While FBPConvNet shows some improvement, the edges and textures remain blurred. HDNet enhances artifact removal and detail recovery, but the internal structure edges are still unclear. NCSN++ and GMSD effectively reduce noise, but excessive smoothing causes blurring of textures and structures. In contrast, our method not only effectively removes artifacts but also preserves rich texture details, resulting in better visual quality, which fully demonstrates its generalization capability and robustness.

#### D. Profile Lines Analysis

In this study, the edge preserving performance of different reconstruction methods is evaluated by comparing the degree



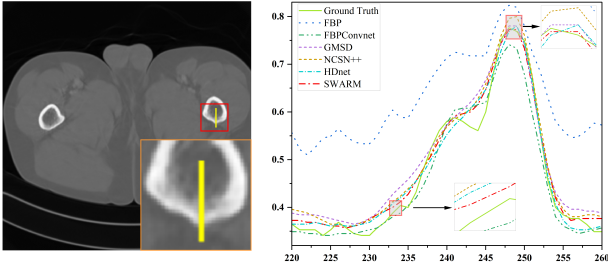


Fig. 5: The intensity profiles of different methods along the specified yellow line in an example reconstructed image.

of matching between the generated contours and the real contours. As shown in Fig. 5, in the comprehensive comparison, the contour generated by SWARM is closer to the real contour, and the contour line is the most accurate. The contours of other methods have poor consistency with the real contours. In addition, in areas with significant gray scale changes, the consistency between the contours generated by SWARM method and the real data is more obvious, which proves its robustness in contour preservation.

TABLE III: Reconstruction Results of AAPM Challenge Data

Methods	Views	PSNR(dB)	SSIM	MSE( $10^{-3}$ )
SHD	30	20.88	0.6448	8.401
	60	24.10	0.7866	3.993
	90	26.02	0.8451	2.567
	120	27.77	0.8885	1.715
SRM	30	31.42	0.9344	0.813
	60	36.44	0.9691	0.253
	90	38.77	0.9772	0.151
	120	40.44	0.9830	0.100
SWARM	30	<b>34.38</b>	<b>0.9585</b>	<b>0.415</b>
	60	<b>38.65</b>	<b>0.9779</b>	<b>0.163</b>
	90	<b>41.76</b>	<b>0.9877</b>	<b>0.070</b>
	120	<b>42.96</b>	<b>0.9901</b>	<b>0.053</b>

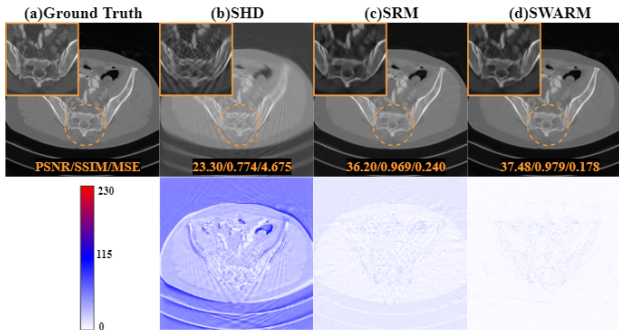


Fig. 6: Reconstruction images obtained from 60 views using different methods. (a) The reference image versus the images reconstructed by (b) SHD, (c) SRM, (d) SWARM. The display window is [0, 230] HU. The second line is the residual between the reference image and the reconstructed image.

### E. Ablation and Generalization Study

To evaluate the effectiveness of each component, we performed ablation experiments on each method. The comprehensiveness and accuracy of the assessment is ensured by testing the impact of each component separately.

1) *Different Components in SWARM Model*: SWARM uses a dual-diffusion model for iterative reconstruction, where SRM is trained using a random mask strategy and SHD is trained based on the random high-frequency components

of the sinogram. Quantitative analysis in Table III shows that SWARM significantly enhances reconstruction. Fig. 6 further illustrates the influence of the model combination, and the qualitative results demonstrate that the cascaded iterative reconstruction of SRM and SHD fully leverages their complementary advantages, significantly improving image reconstruction quality. This demonstrates the effectiveness of our approach, leveraging the strengths of both models to achieve superior reconstruction.

2) *Effectiveness of Random Masking and High-Frequency of Sinogram*: As shown in Table IV and Fig. 7, we study the effects of random masks and randomness based on high-frequency components in the wavelet domain in terms of quantitative indexes and visual effects respectively. NMS is the non-mask for sinogram, and NRH is the non-random wavelet for sinogram. Generalization experiments on the CIRS test set further confirm that the embedded random mask not only greatly improves the generalization ability of the model, but also enhances the robustness of the model, thus verifying the effectiveness of the proposed method. In addition, the training strategy that randomly selects high-frequency components as the input of network training has good stability, effectively enhances the generalization ability of the model, and thus improves the overall reconstruction efficiency.

TABLE IV: Reconstruction Results of CIRS Phantom Data

Methods	Views	PSNR(dB)	SSIM	MSE( $10^{-3}$ )
SHD+NMS	30	25.81	0.9577	2.759
	60	38.06	0.9884	0.159
	90	44.17	0.9956	0.039
	120	46.41	0.9968	0.023
SRM+NRH	30	29.69	0.9529	1.131
	60	37.05	0.9845	0.200
	90	42.84	0.9938	0.053
	120	45.57	0.9959	0.028
SWARM	30	<b>30.58</b>	<b>0.9618</b>	<b>0.899</b>
	60	<b>38.45</b>	<b>0.9886</b>	<b>0.144</b>
	90	<b>44.70</b>	<b>0.9957</b>	<b>0.035</b>
	120	<b>46.68</b>	<b>0.9968</b>	<b>0.022</b>

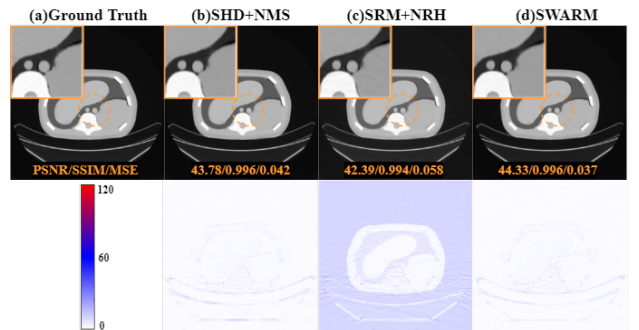


Fig. 7: Reconstruction images obtained from 90 views using different methods. (a) The reference image versus the images reconstructed by (b) SHD+NMS, (c) SRM+NRH, (d) SWARM. The display window is [0, 120] HU. The second line is the residual between the reference image and the reconstructed image.

## V. DISCUSSIONS AND CONCLUSION

In this study, we proposed a diffusion strategy with random masking and high-frequency wavelet decomposition of sinograms for SVCT reconstruction. This method significantly

improved the performance of the model in terms of global consistency and detail reconstruction, thus enhancing the accuracy and reliability of the reconstructed image. Notably, tests conducted on various datasets have validated SWARM's excellent performance in terms of generalization and robustness. However, the proposed method faced certain challenges. The inherent characteristics of the diffusion model led to longer computation times, and the conversion between the projection domain and the wavelet domain added additional computational cost. Future research could explore diffusion models in latent spaces to reduce computational complexity and enhance efficiency while maintaining high performance.

## REFERENCES

- [1] A. M. Cormack, "Representation of a function by its line integrals, with some radiological applications," *J. Appl. Phys.*, vol. 34, no. 9, pp. 2722–2727, 1963.
- [2] G. N. Hounsfield, "Computerized transverse axial scanning (tomography): Part 1. description of system," *Br J Radiol*, vol. 46, no. 552, pp. 1016–1022, 1973.
- [3] T. Wang, W. Xia, *et al.*, "A review of deep learning ct reconstruction from incomplete projection data," *IEEE Trans. Radiat. Plasma Med. Sci.*, vol. 8, no. 2, pp. 138–152, 2024.
- [4] Y. Li, X. Fu, *et al.*, "Sparse-view ct reconstruction with 3d gaussian volumetric representation," *CoRR*, vol. abs/2312.15676, 2023.
- [5] A. P. Dempster *et al.*, "Maximum likelihood from incomplete data via the em algorithm," *J. R. Stat. Soc.*, vol. 39, no. 1, pp. 1–22, 1977.
- [6] D. L. Donoho, "Compressed sensing," *IEEE Trans. Inf. Theory*, vol. 52, no. 4, pp. 1289–1306, 2006.
- [7] S. Emil Y, X. Pan, *et al.*, "Image reconstruction in circular cone-beam computed tomography by constrained, total-variation minimization," *Phys. Med. Biol.*, vol. 53, no. 17, pp. 4777–4807, 2008.
- [8] H. Yu and G. Wang, "Compressed sensing based interior tomography," *Phys. Med. Biol.*, vol. 54, no. 9, pp. 2791–2805, 2009.
- [9] O. Rioul and M. Vetterli, "Wavelets and signal processing," *IEEE Trans. Inf. Theory*, vol. 8, no. 4, pp. 14–38, 1991.
- [10] Y. S. Han, J. Yoo, *et al.*, "Deep residual learning for compressed sensing ct reconstruction via persistent homology analysis," *CoRR*, vol. abs/1611.06391, 2016.
- [11] Z. Zhang, X. Liang, *et al.*, "A sparse-view ct reconstruction method based on combination of densenet and deconvolution," *IEEE Trans. Med. Imaging*, vol. 37, no. 6, pp. 1407–1417, 2018.
- [12] L. R. Koetzier, D. Mastrodicasa, *et al.*, "Deep learning image reconstruction for ct: Technical principles and clinical prospects?" *RADIOLOGY*, vol. 306, no. 3, 2023.
- [13] J. Zhong, Z. Wu, *et al.*, "Impacts of adaptive statistical iterative reconstruction-v and deep learning image reconstruction algorithms on robustness of ct radiomics features: Opportunity for minimizing radiomics variability among scans of different dose levels," *J. Imaging Inform. Med.*, pp. 1–11, 2024.
- [14] M. T. McCann, K. H. Jin, *et al.*, "Deep convolutional neural network for inverse problems in imaging," *IEEE Trans. Image Process.*, vol. 26, no. 9, pp. 4509–4522, 2017.
- [15] H. Chen, Y. Zhang, *et al.*, "Low-dose ct with a residual encoder-decoder convolutional neural network," *IEEE Trans. Med. Imaging*, vol. 36, no. 12, pp. 2524–2535, 2017.
- [16] Q. Zhang, Z. Hu, *et al.*, "Artifact removal using a hybrid-domain convolutional neural network for limited-angle computed tomography imaging," *Phys. Med. Biol.*, vol. 65, no. 15, p. 155010, 2020.
- [17] J. Pan, H. Zhang, *et al.*, "Multi-domain integrative swin transformer network for sparse-view tomographic reconstruction," *PATTERNS*, vol. 3, no. 6, 2022.
- [18] D. Hu, J. Liu, *et al.*, "Hybrid-domain neural network processing for sparse-view ct reconstruction," *IEEE T. Radiat. Plasma Med. Sci.*, vol. 5, no. 1, pp. 88–98, 2021.
- [19] W. Xia, W. Cong, *et al.*, "Patch-based denoising diffusion probabilistic model for sparse-view ct reconstruction," *CoRR*, 2022.
- [20] W. Wu and Y. Wang, "Data-iterative optimization score model for stable ultra-sparse-view ct reconstruction," *CoRR*, vol. abs/2308.14437, 2023.
- [21] B. Guan, C. Yang, *et al.*, "Generative modeling in sinogram domain for sparse-view ct reconstruction," *IEEE T. Radiat. Plasma Med. Sci.*, vol. 8, no. 2, pp. 195–207, 2023.
- [22] W. Xia, H. W. Tseng, *et al.*, "Parallel diffusion model-based sparse-view cone-beam breast ct," 2024. [Online]. Available: <https://arxiv.org/abs/2303.12861>
- [23] C. Yang, D. Sheng, *et al.*, "A dual-domain diffusion model for sparse-view ct reconstruction," *IEEE Trans. Image Process.*, vol. 31, pp. 1279–1283, 2024.
- [24] A. Kazerouni, E. K. Aghdam, *et al.*, "Diffusion models for medical image analysis: A comprehensive survey," 2023. [Online]. Available: <https://arxiv.org/abs/2211.07804>
- [25] J. Ho, A. Jain, *et al.*, "Denoising diffusion probabilistic models," 2020. [Online]. Available: <https://arxiv.org/abs/2006.11239>
- [26] M. Aversa, G. Nobis, *et al.*, "Diffinfinite: Large mask-image synthesis via parallel random patch diffusion in histopathology," 2023. [Online]. Available: <https://arxiv.org/abs/2306.13384>
- [27] A. Toker, M. Eisenberger, *et al.*, "Satsynth: Augmenting image-mask pairs through diffusion models for aerial semantic segmentation," 2024. [Online]. Available: <https://arxiv.org/abs/2403.16605>
- [28] N. Konz, Y. Chen, *et al.*, "Anatomically-controllable medical image generation with segmentation-guided diffusion models," 2024. [Online]. Available: <https://arxiv.org/abs/2402.05210>
- [29] P. Tan, M. Geng, *et al.*, "Msdiff: Multi-scale diffusion model for ultra-sparse view ct reconstruction," *arXiv preprint arXiv:2405.05814*, 2024.
- [30] Y. Song, L. Shen, *et al.*, "Solving inverse problems in medical imaging with score-based generative models," *arXiv preprint arXiv:2111.08005*, 2021.
- [31] Y. Song and S. Ermon, "Generative modeling by estimating gradients of the data distribution," *Adv. Neural Inf. Process. Syst.*, vol. 32, pp. 11 895–11 907, 2019.
- [32] Y. Song, J. Sohl-Dickstein, *et al.*, "Score-based generative modeling through stochastic differential equations," *arXiv preprint arXiv:2011.13456*, 2020.
- [33] H. Wang, S. P. H. Boroujeni, *et al.*, "Flame diffuser: Wildfire image synthesis using mask guided diffusion," *arXiv preprint arXiv:2403.03463*, 2024.
- [34] S. Gao, P. Zhou, *et al.*, "Masked diffusion transformer is a strong image synthesizer," in *Proc. IEEE/CVF Int. Conf. Comput. Vis.*, 2023, pp. 23 164–23 173.
- [35] M. Aversa, G. Nobis, *et al.*, "Diffinfinite: Large mask-image synthesis via parallel random patch diffusion in histopathology," *NeurIPS*, vol. 36, pp. 78 126–78 141, 2024.
- [36] G. Couairon, J. Verbeek, *et al.*, "Diffedit: Diffusion-based semantic image editing with mask guidance," *arXiv preprint arXiv:2210.11427*, 2022.
- [37] Q. Wang, B. Zhang, *et al.*, "Instructedit: Improving automatic masks for diffusion-based image editing with user instructions," *arXiv preprint arXiv:2305.18047*, 2023.
- [38] S. Zou, J. Tang, *et al.*, "Towards efficient diffusion-based image editing with instant attention masks," in *AAAI Conf. Artif. Intell.*, vol. 38, no. 7, 2024, pp. 7864–7872.
- [39] Y. Pang, J. Mao, *et al.*, "An improved face image restoration method based on denoising diffusion probabilistic models," *IEEE Access*, pp. 3581–3596, 2024.
- [40] Y. Zhu, K. Zhang, *et al.*, "Denoising diffusion models for plug-and-play image restoration," in *Proc. IEEE/CVF Conf. Comput. Vis. Pattern Recognit.*, 2023, pp. 1219–1229.
- [41] M.-Q. Le, T. V. Nguyen, *et al.*, "Maskdiff: Modeling mask distribution with diffusion probabilistic model for few-shot instance segmentation," in *AAAI Conf.*, vol. 38, no. 3, 2024, pp. 2874–2881.
- [42] A. Toker, M. Eisenberger, *et al.*, "Satsynth: Augmenting image-mask pairs through diffusion models for aerial semantic segmentation," in *CVPR*, 2024, pp. 27 695–27 705.
- [43] A. Moloud, P. Farhad, *et al.*, "A review of uncertainty quantification in deep learning: Techniques, applications and challenges," *Information Fusion*, vol. 76, pp. 243–297, 2021.
- [44] "Low dose ct grand challenge." Available: <http://www.aapm.org/GrandChallenge/LowDoseCT/>, 2017.
- [45] H. Lee, S. Yune, *et al.*, "An explainable deep-learning algorithm for the detection of acute intracranial haemorrhage from small datasets," *Nat. Biomed. Eng.*, vol. 3, pp. 173–182, 2019.
- [46] W. L. Bi, A. Hosny, *et al.*, "Artificial intelligence in cancer imaging: Clinical challenges and applications," *CA Cancer J Clin.*, vol. 69, pp. 127–157, 02 2019.
- [47] P. Rajpurkar, E. Chen, *et al.*, "Ai in health and medicine," *Nat. Med.*, vol. 28, no. 1, pp. 31–38, 2022.
- [48] D. J. Brenner and E. J. Hall, "Computed tomography—an increasing source of radiation exposure," *N. Engl. J. Med.*, vol. 357, no. 22, pp. 2277–2284, 2007.